THE JOURNAL OF PHYSICAL CHEMISTRY C

pubs.acs.org/JPCC Article

Direct Experimental Evidence of Hot Carrier-Driven Chemical Processes in Tip-Enhanced Raman Spectroscopy (TERS)

Rui Wang, Jingbai Li, Joel Rigor, Nicolas Large, Patrick Z. El-Khoury, Andrey Yu. Rogachev, and Dmitry Kurouski*

Cite This: https://dx.doi.org/10.1021/acs.jpcc.9b12002 Read Online

ACCESS | Metrics & More | Article Recommendations | Supporting Information

ABSTRACT: Nanoscale localization of electromagnetic fields using metallic nanostructures can catalyze chemical reactions in their immediate vicinity. Local optical field confinement and enhancement is also exploited to attain single-molecule detection sensitivity in surface- and tip-enhanced Raman (TER) spectroscopy. In this work, we observe and investigate the sporadic formation of 4-nitrobenzenethiolate upon TER imaging of a 4-nitrobenzenethiol (4NBT) monolayer on Au(111). Density functional theory (DFT), finite-difference time-domain (FDTD), and finite element method (FEM) calculations together confirm that this chemical reaction does not occur as a result of thermal desorption of the molecule, which requires temperatures in excess of 2100 K at the tip−sample junction. Our combined experimental and theoretical analyses strongly suggest that the chemical transformations observed throughout the course of TERS mapping is not driven by plasmonic photothermal heating, but rather by plasmon-induced hot carriers.

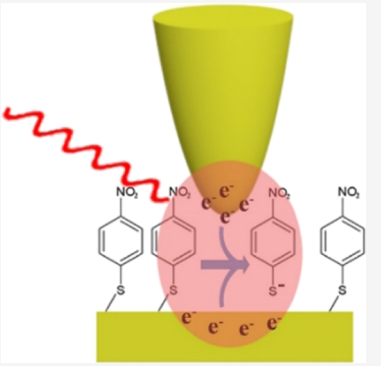

INTRODUCTION

The resonant interaction between noble metal nanostructures and electromagnetic radiation induces coherent, collective oscillations of the conduction electrons at the metal surface.[1−3] In their spatially confined variants, these oscillations, also known as localized surface plasmon resonances (LSPRs), account for an extremely large enhancement (up to 10^8) of Raman scattering from molecules at the nanostructure surface.[4,5] This effect is perhaps most evident in surface-enhanced Raman spectroscopy (SERS), a technique that routinely allows the observation and identification of single analytes.[6,7]

Exciting surface plasmons may also lead to the formation of hot carriers through direct interband, phonon-assisted intraband, and geometry-assisted transitions.[8−10] These hot carriers are highly energetic species, and they persist over a few tens of femtoseconds to picoseconds time scale.[11,12] They can decay via electron−electron or electron−phonon scattering or can populate unoccupied orbitals in molecules located at the metal surface.[13,14] In the latter scenario, hot carriers can catalyze chemical reactions, such as O_2 and H_2 dissociation.[15,16]

The community has actively used SERS substrates to investigate the mechanisms of plasmon-driven chemical reactions. For instance, Christopher et al. investigated the mechanisms of ethylene epoxidation on Ag nanoparticles.[17] Other reports investigated the oxidation of 4-nitrobenzenethiol (4NBT),[18] phenyl isocyanide,[19] photodissociation of dimethyl disulfide,[20] demethylation of methylene blue,[21] and the dehydroxylation of *p*-hydroxythiophenol.[22]

Plasmon-driven chemical reactions have also been observed on plasmonic systems with a single electromagnetic hot-spot.[23] Such systems are strongly reminiscent of the gap-mode tip-enhanced Raman spectroscopy (TERS) scheme.[24] More generally, in TERS, noble metal nanostructures are grown or electrochemically etched at the apex of a scanning probe.[25,26] van Schrojenstein Lantmanvan et al. demonstrated that Ag-coated tips may be used to photocatalytically convert *p*-nitrothiophenol adsorbed on gold nanoplates to *p*,*p*′-dimercaptoazobisbenzene (DMAB).[27] It has also been shown that the N═N bond of DMAB could be scissored by hot carriers with the formation of 4NBT at alkaline and *p*-aminothiophenol at acidic pH.[28] Szczerbiński et al. used TERS to monitor photocatalytic degradation of 1-hexadecanethiol, biphenyl-4-thiol, and 1H,1H,2H,2H-perfluorodecane-1-thiol.[29] They demonstrated that illumination of the tip−sample junction by high laser power (>1 mW) causes the formation of carbonaceous species via charge-driven reaction mechanisms. At the same time, there are numerous TERS constructs that do not support plasmon-enhanced chemical transformations.[18,19,30,31] This raises several important fundamental questions, including how frequently do these hot carrier events occur in TERS?

Received: December 29, 2019
Published: January 2, 2020

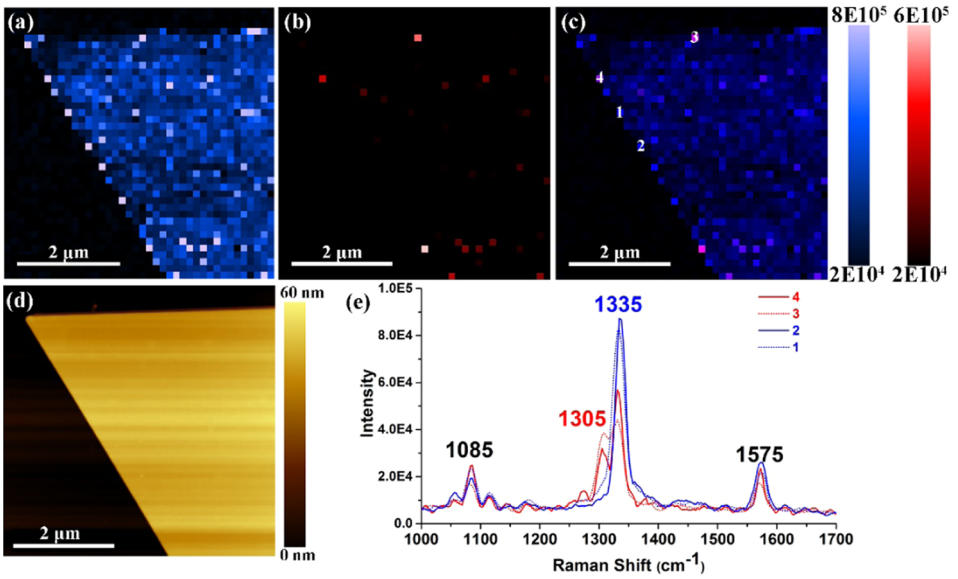

Figure 1. TER images of a 4NBT monolayer on the gold Au (111) surface. (a, b) are based on the integral intensities of the spectrum from 1320 to 1350 cm^{-1} (a) and 1290 to 1320 cm^{-1} (b), respectively. (c) Overlapped image of (a, b). (d) Corresponding AFM image of the area from which TER images were taken. (e) Typical TER spectra extracted from the marked position in (c). The scanning step is 20 nm per pixel.

RESULTS

To this end, we perform careful measurements of the vibrational properties of a 4NBT monolayer on a Au(111) surface. We use minimal low laser power (P = 60 μW, λ = 671 nm) to ensure the integrity of the tip and sample. Measurements were performed using a side-illumination geometry with an Au tip (cone diameter = 50 nm). TER imaging of this seemingly simple chemical system revealed two types of vibrational spectra (Figure 1). The vast majority of spectra exhibited vibrational bands that were typical of 4NBT, whereas a very small fraction of spectra had the 1335 cm^{-1} band shifted to 1305 cm^{-1} (Figure 1e).

We used density functional theory (DFT) calculations to determine structural and possible electronic changes in 4NBT that would result in the observed shift of the 1335 cm^{-1} band observed upon TER imaging. Our theoretical investigation was driven by the hypothesis that the observed shift (1335−1305 cm^{-1}) could indicate the formation of a 4NBT anion. Comparison of neutral and anionic species revealed the synergetic reduction of the C−N bond distance and elongation of the N−O bond. Such changes in geometry can be undoubtedly considered as consequences of adding one electron to the lowest unoccupied molecular orbital (LUMO) of 4NBT. It is clear that the LUMO (Figure 2a) possesses a great bonding character between the 4NBT and the NO_2 group. The π orbital is highly overlapping with the p_z orbital of the nitrogen (with the z-axis perpendicular to the benzene ring). Thus, adding an electron to the LUMO orbital would be expected to increase the bonding character of the C−N bond and result in a shorter bond distance. On the other hand, the antibonding mixing of the p_z orbital of the N and O atoms is also noticeable. Two nodal planes just intersect the O−N bonds, which weakens the N−O bond that is noticeably longer in the anion form. The results of DFT calculations (Figure 2b) showed that in the Raman spectrum of the 4NBT anion, C−S vibration shifted from 1087 cm^{-1} (NBT) to 1082 cm^{-1} (anion). N−O vibration also exhibited a shift from 1307

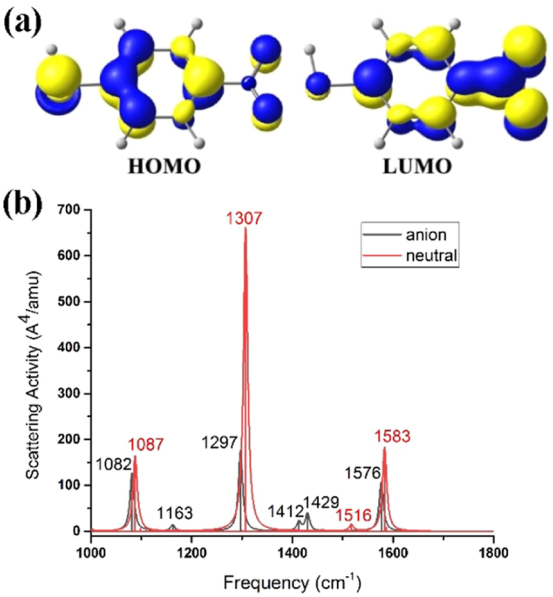

Figure 2. DFT calculation on the neutral 4NBT and its anion. (a) Highest occupied molecular orbital (HOMO) and lowest unoccupied molecular orbital (LUMO) of 4NBT. (b) PBE/def2-TZVP Raman spectra of 4NBT (red; also see refs 27, 32) and its anionic analog (black) in the 1000−1800 cm^{-1} spectral range. Peak assignments are also shown in their corresponding colors. These calculations were performed using NWChem.[33]

cm^{-1} (4NBT) to 1297 cm^{-1} (anion), as well as C−C vibration from 1087 cm^{-1} (4NBT) to 1082 cm^{-1} (anion), Table 1.

It should be noted that similar blue shifts were observed in the Raman spectrum of ethanolic 4NBT when the pH was increased (Figure S1). This observation suggests that the blue shift was caused by the deprotonation of the thiol group in the 4NBT.[34] These experimental and theoretical findings together indicate that the observed TERS spectral changes correspond to the formation of the 4NBT anion. Using plasmon-enhanced Raman scattering, the Schultz group demonstrated that large

https://dx.doi.org/10.1021/acs.jpcc.9b12002
J. Phys. Chem. C XXXX, XXX, XXX−XXX

Table 1. Selected Raman Active Vibrational Modes in Neutral 4NBT and its Anion

mode	experimental (cm^{-1})	neutral (cm^{-1})	anion (cm^{-1})
C−S	1085	1087	1082
C−N	1120		1163
N−O	1305, 1335	1307	1297
C−C	1575	1583	1576

electric fields at plasmonic nanojunctions can cause shifts in the recorded vibrational frequencies of nitrile groups[35] as a result of the vibrational Stark effect.[36,37] We used DFT calculations to investigate the possibility of electric field-induced shifts in the N−O vibrational resonance. Our results show that a field of ∼140 MV cm^{-1} is required to shift the N−O vibration from 1333 to 1305 cm^{-1} (Figure S2), which is unlikely to be achieved in the TERS geometry under our experimental conditions. To support our calculations, we repeated the measurements described in the main text, but now, using 4-mercaptobenzonitrile as a molecular TERS reporter, to gauge the absolute magnitude of the local optical fields in the TERS geometry.[38−41] We follow the protocol outlined in a prior SERS study that employed the same reporter to quantify the magnitude of rectified (DC) fields that are generated at plasmonic gold nanoparticle−gold surface nanojunctions.[42] In addition to the normal Raman signature of the nitrile (2225 cm^{-1}), we observe several additional peaks at lower frequencies, which may be assigned to Stark-shifted nitrile resonances (Figure S3).[42,43] The lowest nitrile resonance frequency we observed is centered at ∼2200 cm^{-1}. Using the literature-reported Stark tuning rate for our reporter (∼0.6 cm^{-1}/MV cm^{-1}), we can set an upper limit for the magnitude of the rectified local field in our geometry (∼42 MV cm^{-1}). Therefore, we can exclude this possibility on the basis of our calculations and measurements.

Next, we explored molecular orientation-dependent Raman scattering to investigate whether the observed spectral changes may arise from molecular (re)orientation at the plasmonic tip−sample junction. We followed the procedure outlined in a recent report.[32] Our results reveal that a change in molecular orientation merely affects the relative intensities of the observable vibrational eigenstates. For instance, going from orthogonal to parallel (relative to the metal surface) causes an increase in the intensity of the 1087 cm^{-1} band relative to the 1307 cm^{-1} band (C−S) or near complete dimming of the 1307 cm^{-1} band (N−O) (Figure S4). At the same time, no spectral shift in the N−O vibrational peak was observed.

One can envision that the formation of the 4NBT anion from 4NBT on the Au surface is energetically unfavorable. It would require breaking the Au−S bond, which could occur either as a result of thermal desorption or via hot carrier injection. To shed some light on this possibility, we calculated the energetics of the Au−S bond in the 4NBT−Au complex and the required temperature for its breakage. The absorption model, $[(C_6H_4NO_2S)-(Au_{12})]$, was constructed by placing the deprotonated 4NBT ($C_6H_4NO_2SH$) on a single layer of Au(111) with 12 atoms. The Au−Au distance was set to 2.915 Å, obtained by optimization of an fcc lattice of bulk Au at the PBE/TZ2P level of theory.[44] The Au lattice was optimized using the ADFBAND2018 program suite. The optimization for the model complex was then performed at the PBE0/Def2-TZVP level of theory with a constrained Au(111) surface. The "resolution-of-identity" (RI)[45] approximation to the Coulomb term and the auxiliary basis set for Coulomb fitting were used to speed up integration of electronic density.[46,47]

The Gibbs free energy ranging from 290 to 1000 K was calculated. All results were obtained with help of ORCA 4.0.0 program. We considered the heterolytic dissociation of the Au−S bond to evaluate the stability of the absorption model

$$\Delta G_{\text{absorption model}} = G(C_6H_4NO_2Au_{12}) - G(C_6H_4NO_2^{-}) - G(Au_{12}^{+}) \quad (1)$$

On the other hand, one can also inspect the energy barrier of the Au−S bond breaking, thus providing information about its kinetic stability. For the sake of comparison, we followed the same expression to evaluate the relative energy of the transition state to reveal the influence of temperature

$$\Delta E_a = G(TS) - G(C_6H_4NO_2Au_{12}) \quad (2)$$

Calculations of the Gibbs free energy showed a linear correlation between the temperature and the relative energy. One can easily notice that, as the temperature increases, the stability of adsorption model decreases, which follows a linear equation

$$\Delta G_{\text{adsorption model}} = 0.05 \cdot T - 107.15 \quad (3)$$

where T is the temperature in kelvin. When the temperature is higher than ∼2100 K, the complex turns out to be thermodynamically unstable ($\Delta G > 0$). These findings indicate that thermal desorption of 4NBT from the Au surface, which would result in breaking of the Au−S bond, could occur at ∼2100 K.

It is highly unlikely that such high temperatures can be reached at the tip−substrate junction under our experimental conditions. Nonetheless, we use the finite-difference time-domain (FDTD)[48] and the finite element method (FEM)[49] to calculate the optical and photothermal properties of our TERS system. To estimate the plasmonic heating effects, we begin by finding the heat power (or absorbed power), which is defined by

$$Q = \sigma_{abs} I \quad (4)$$

where σ_{abs} is the absorption cross-section of the system and I is the irradiance of the optical excitation (power per unit surface). Q acts as a heat source that induces an increase in the local temperature

$$\Delta T(r) = \frac{Q}{4\pi_0 R_{tip} + r} \quad (5)$$

where κ_0 is defined as the thermal conductivity of the surrounding medium, R_{tip} is the tip radius, and r is the distance from the metal surface. Though this model gives us a good approximation of what should be expected in the system, it is better to solve the heat-transfer equation using FEM

$$\rho(\mathbf{r}) c_p(\mathbf{r}) \frac{\partial T(\mathbf{r}, t)}{\partial t} - \nabla[\kappa(\mathbf{r}) \nabla T(\mathbf{r}, t)] = q(\mathbf{r}) \quad (6)$$

where ρ is the mass density, c_p is the specific heat, and κ is the thermal conductivity. The function $q(\mathbf{r})$ is the applied heat energy transfer rate (or heat power density) inside the metal such that $Q = \int_V q(\mathbf{r}) d^3r$, where the integral runs over the volume V of the plasmonic system. It represents a heat source coming from the dissipation of the optical energy through Joule effect. Given that the calculations are performed in the

https://dx.doi.org/10.1021/acs.jpcc.9b12002
J. Phys. Chem. C XXXX, XXX, XXX−XXX

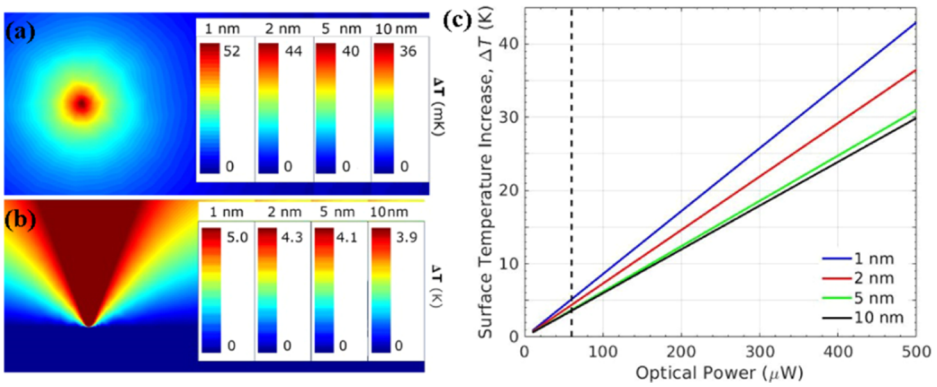

Figure 3. Simulation of the thermal effect caused by the tip. Temperature profiles calculated for an optical excitation of 671 nm (a) on the substrate and (b) at the tip−substrate junction for tip−substrate distances of 1, 2, 5, and 10 nm. (c) Tip surface temperature dependency on the optical power for tip−substrate distances of 1, 2, 5, and 10 nm. The black dashed line indicates the experimental excitation of 60 μW.

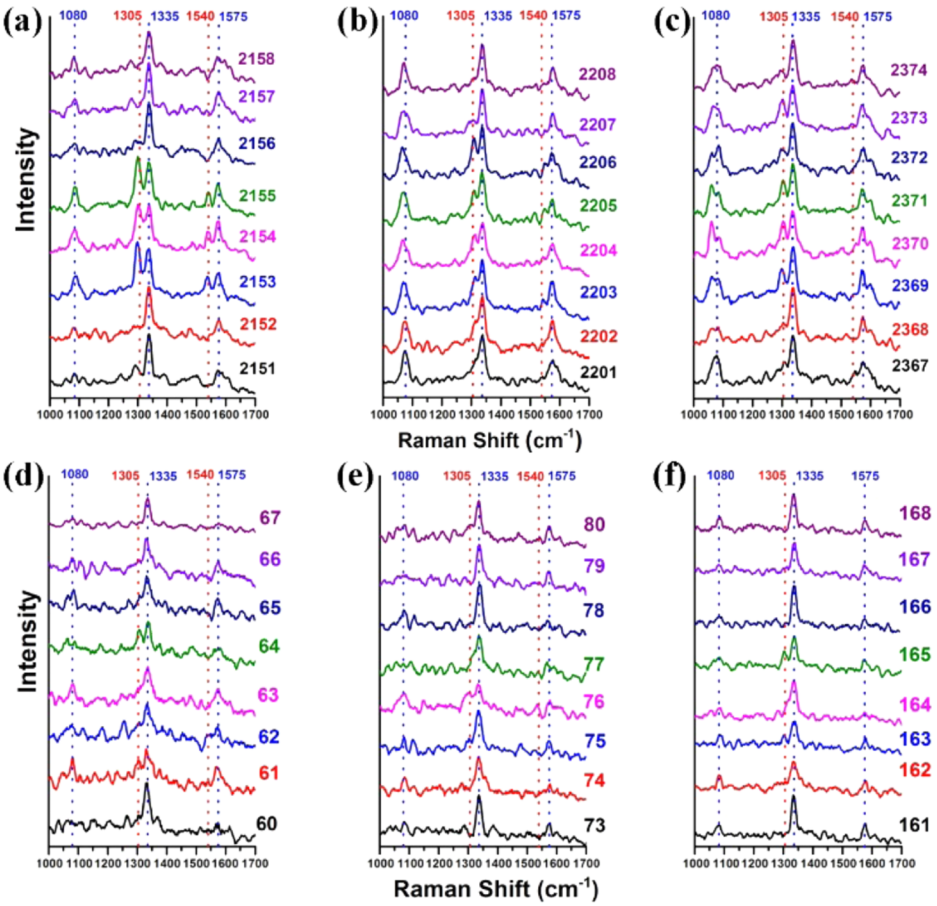

Figure 4. Selected TER spectra showing the appearance of the 1305 cm^{-1} peak. TER spectra of 4NBT on the Au surface collected by two different probes (top and bottom rows). Numbers indicate the location of the spectra on the TERS map that is shown in Figure S6.

steady state $\left(\frac{\partial T}{\partial t} = 0\right)$, the equation is reduced to a Poisson's equation

$$\nabla[\kappa(\mathbf{r})\nabla T(\mathbf{r}, t)] = -q(\mathbf{r}) \quad (7)$$

The establishment of the steady-state temperature profile is usually very fast when working with nanoscale systems. Under continuous wave illumination, the typical duration τ_{tr} of the transient regime is not dependent on the temperature increase but on the characteristic size of the system. For a micron-scale metallic tip τ_{tr} is of the order of microseconds.

Our modeled TERS systems are comprised of a gold tip and a semi-infinite gold substrate, with the distance between the tip and substrate varying from 1 to 10 nm. We first investigate the LSPR of each system to quantify the optical properties. To determine the LSPR of the TERS system, we calculate the absorption cross-section, σ_{abs}, using FDTD (Figure S5). We use the absorption to calculate the heat power (eq 4), which is then used as the heat source in the FEM calculations (eqs 6 and 7).

Looking at the spectra, we do not see any defined shift in the LSPR when comparing all of the TERS systems at 1, 2, 5, and

https://dx.doi.org/10.1021/acs.jpcc.9b12002
J. Phys. Chem. C XXXX, XXX, XXX−XXX

10 nm. The LSPR is located at a wavelength of ∼530 nm for each individual system. The excitation wavelength (671 nm) is off resonance with respect to the LSPR of each of the TERS system (Figure S5). Because of the off-resonance excitation, we expect drastically lower temperatures than at the LSPR. Also looking at the absorption spectra, we expect the magnitude of the temperature change at 671 nm to be similar for tip−junction distances in the range 1−10 nm.

Temperature profiles are calculated using FEM for different TERS systems excited at 671 nm at varying tip−substrate distances of 1, 2, 5, and 10 nm and an input power of 60 μW, corresponding to an irradiance I = 0.375 mW μm^{-2}. Figure 3a shows the change in temperature to be in the range of 36−52 mK at the surface of the substrate. It shows that, as the tip gets further away from the substrate, the maximum local temperature increase ΔT is lower, and the same for the temperature profiles of the tip−substrate junction for various tip distances (Figure 3b). Here, we see that the tip is the hottest part of the system and the changes in temperature are 100 times greater on the tip (3.9−5.0 K) than on the substrate (36−52 mK).

We also note that this maximum temperature is found in the system with the smallest tip−substrate distance of 1 nm. This is due to the metallic nature of both the tip and the substrate. Indeed, as the tip−substrate distance deceases, the electromagnetic interactions increase within the tip−substrate junction, as shown through the increase in the absorption cross-section (inset, Figure S5). Additionally, we performed FDTD−FEM simulations for increasing incident optical power to estimate the range of temperature increase. We used input powers ranging from 10 to 500 μW on the TERS system, with tip−substrate distances varying from 1 to 10 nm (Figure 3c). The maximum local temperature, observed at the tip surface, scales linearly with the input power. The 1 nm tip−substrate distance exhibits the largest change in surface temperature across all input powers when compared to the other systems (43 K at P = 0.5 mW). With the calculations of the Gibbs free energy, one can see that the system becomes thermodynamically unstable at higher temperatures (∼2100 K). We see that none of the systems we have modeled achieve temperatures higher than ∼305 K at 60 μW and up to 343 K at 0.5 mW. Temperatures around this magnitude are not enough to be responsible for the decomposition reaction of 4NBT on the gold surface. Therefore, these results suggest that the formation of 4NBT anions observed in the TERS experiments is a plasmon-driven process, which takes place upon injection of hot carriers in the Au−S bond.

We collected 2500 TER spectra across the monolayer of 4NBT on the Au surface to understand the relative abundance of the anionic species in the TERS geometry. The integrated time of each spectrum and the excitation power was 0.5 s (60 μW). It should be pointed out that the TERS tip experienced a full round of contacting and retracting for each spectral acquisition, which is very effective in avoiding tip contamination or tip-induced photocatalysis. We have found that the fraction of the 1305 cm^{-1} peak was less than 1% of the total spectra for both these TERS probes, which means that these thiolate species were very rare. Interestingly, we can observe the gradual increase and disappearance process of the 1305 cm^{-1} peak in some consecutive spectra imaged by a TERS probe (Figures 4 and S6). In some cases, there was a notable 1540 cm^{-1} peak appearing along with the rise of the 1305 cm^{-1} peak, like spectra nos. 2153−2155 in Figure 4a.

DISCUSSION

This work confirmed the previously proposed possibility for hot carrier-mediated desorption reactions that could take place on metallic surfaces together with well-studied photochemical reactions.[50,51] However, the observed reaction is not a pure hot carrier-driven physidesorption process, which was previously observed for carbon monoxide.[52] The 4NBT hot carrier desorption is determined by reduction of the Au−S bond and one can envision that such hot carrier-driven reduction can be induced by the indirect hot electron-transfer mechanism and the direct intramolecular excitation mechanism. Although detailed mechanisms of such hot carrier-driven reactions have to be fully understood, we believe that the physics of these processes is drastically different from previously reported photon-driven desorption of adsorbates from metal surfaces. These photon-driven reactions are based on ejection of electrons from the metal surface upon its illumination by electromagnetic radiation. First observed by Hertz,[53] this phenomenon was explained by Einstein[54] and is currently known as the photoelectric effect. The physics of photon-driven desorption reactions was well characterized in excellent works by Gadzuk and co-workers.[55−57] It was proposed that photons caused ejection of electrons from the metal, with their subsequent injection into LUMO of the adsorbate located on the metal surface and back transfer of the electron to the metal. Such processes could occur only if the photon energy is above the Fermi energy of the metal. In our experiments, 671 nm laser light is used, which corresponds to 1.85 eV, whereas the Fermi energy of gold is 5.51 eV (T = 293 K).[57] Thus, the observed thiolate formation can be attributed to hot carrier-driven rather than photon-driven physics.

CONCLUSIONS

We performed a careful spectroscopic investigation to detect hot carrier-driven processes in TERS. Using TERS, we analyzed a monolayer of 4NBT on Au nanoplates. We found that a small fraction of the spectra (less than 1%) exhibited vibrational bands that could be assigned to 4NBT thiolate. The formation of this anionic species could occur either as a result of its thermal desorption from the Au surface or as a result of hot carrier injection into the LUMO of 4NBT. DFT calculations indicate that thermal desorption of 4NBT could occur only at temperatures above 2100 K. Combined FDTD−FEM calculations demonstrated that our experimental conditions (λ = 671 nm, P = 60 μW) induce a modest temperature increase in the tip−sample junction that does not exceed 305 K. These results exclude the possibility of thermal desorption of 4NBT from the Au surface, strongly suggesting that the observed thiolate formation occurred via plasmon-induced hot carrier-driven processes.

ASSOCIATED CONTENT

Supporting Information

The Supporting Information is available free of charge at https://pubs.acs.org/doi/10.1021/acs.jpcc.9b12002.

Synthesis of a Au microplate with Au (111) as basal facets; preparation of the 4NBT monolayer on Au (111); TERS probes' fabrication; TERS measurement parameters; FEM and FDTD modeling details; DFT calculations; Raman spectra of 4NBT ethanolic solution; Stark effect on the peak frequencies; TER images; tip−

https://dx.doi.org/10.1021/acs.jpcc.9b12002
J. Phys. Chem. C XXXX, XXX, XXX−XXX

substrate distance-dependent absorption cross sections (PDF)

AUTHOR INFORMATION

Corresponding Author

Dmitry Kurouski − *Texas A&M University, College Station, Texas;* orcid.org/0000-0002-6040-4213; Email: dkurouski@tamu.edu

Other Authors

Rui Wang − *Texas A&M University, College Station, Texas;* orcid.org/0000-0002-9452-9241

Jingbai Li − *Illinois Institute of Technology, Chicago, Illinois*

Joel Rigor − *The University of Texas at San Antonio, San Antonio, Texas*

Nicolas Large − *The University of Texas at San Antonio, San Antonio, Texas;* orcid.org/0000-0002-2699-5718

Patrick Z. El-Khoury − *Pacific Northwest National Laboratory, Richland, Washington;* orcid.org/0000-0002-6032-9006

Andrey Yu. Rogachev − *Illinois Institute of Technology, Chicago, Illinois;* orcid.org/0000-0001-9855-7824

Complete contact information is available at: https://pubs.acs.org/10.1021/acs.jpcc.9b12002

Notes

The authors declare no competing financial interest.

ACKNOWLEDGMENTS

R.W. and D.K. are grateful to AgriLife Research of Texas A&M for providing financial support. They also acknowledge the Governor's University Research Initiative (GURI) grant program of Texas A&M University, GURI Grant Agreement No. 12-2016, M1700437. J.R. and N.L. acknowledge the financial support from the Army Research Office (ARO) under Grant Number W911NF-18-1-0439. P.Z.E. acknowledges support from the U.S. DOE, Office of Science, Office of Basic Energy Sciences, Division of Chemical Sciences, Geosciences & Biosciences. This work received computational support from UTSA's HPC cluster Shamu, operated by the Office of Information Technology.

REFERENCES

(1) Wustholz, K. L.; Henry, A.-I.; McMahon, J. M.; Freeman, R. G.; Valley, N.; Piotti, M. E.; Natan, M. J.; Schatz, G. C.; Van Duyne, R. P. Structure−Activity Relationships in Gold Nanoparticle Dimers and Trimers for Surface-Enhanced Raman Spectroscopy. *J. Am. Chem. Soc.* **2010**, *132*, 10903−10910.

(2) Ringe, E.; McMahon, J. M.; Sohn, K.; Cobley, C.; Xia, Y.; Huang, J.; Schatz, G. C.; Marks, L. D.; Van Duyne, R. P. Unraveling the Effects of Size, Composition, and Substrate on the Localized Surface Plasmon Resonance Frequencies of Gold and Silver Nanocubes: A Systematic Single-Particle Approach. *J. Phys. Chem. C* **2010**, *114*, 12511−12516.

(3) Kurouski, D.; Large, N.; Chiang, N.; Greeneltch, N.; Carron, K. T.; Seideman, T.; Schatz, G. C.; Van Duyne, R. P. Unraveling near-Field and Far-Field Relationships for 3D SERS Substrates − A Combined Experimental and Theoretical Analysis. *Analyst* **2016**, *141*, 1779−1788.

(4) King, F. W.; Van Duyne, R. P.; Schatz, G. C. Theory of Raman Scattering by Molecules Adsorbed on Electrode Surfaces. *J. Chem. Phys.* **1978**, *69*, 4472−4481.

(5) Moskovits, M. Surface Roughness and the Enhanced Intensity of Raman Scattering by Molecules Adsorbed on Metals. *J. Chem. Phys.* **1978**, *69*, 4159−4161.

(6) Kneipp, K.; Wang, Y.; Kneipp, H.; Perelman, L. T.; Itzkan, I.; Dasari, R. R.; Feld, M. S. Single Molecule Detection Using Surface-Enhanced Raman Scattering (SERS). *Phys. Rev. Lett.* **1997**, *78*, No. 1667.

(7) Nie, S.; Emory, S. R. Probing Single Molecules and Single Nanoparticles by Surface-Enhanced Raman Scattering. *Science* **1997**, *275*, 1102−1106.

(8) Khurgin, J. B. How to Deal with the Loss in Plasmonics and Metamaterials. *Nat. Nanotechnol.* **2015**, *10*, 2−6.

(9) Narang, P.; Sundararaman, R.; Atwater, H. A. Plasmonic Hot Carrier Dynamics in Solid-State and Chemical Systems for Energy Conversion. *Nanophotonics* **2016**, *5*, 96−111.

(10) Manjavacas, A.; Liu, J. G.; Kulkarni, V.; Nordlander, P. Plasmon-Induced Hot Carriers in Metallic Nanoparticles. *ACS Nano* **2014**, *8*, 7630−7638.

(11) Brown, A. M.; Sundararaman, R.; Narang, P.; Goddard, W. A., III; Atwater, H. A. Nonradiative Plasmon Decay and Hot Carrier Dynamics: Effects of Phonons, Surfaces, and Geometry. *ACS Nano* **2016**, *10*, 957−966.

(12) Hartland, G. V. Optical Studies of Dynamics in Noble Metal Nanostructures. *Chem. Rev.* **2011**, *111*, 3858−3887.

(13) Ma, J.; Wang, Z.; Wang, L.-W. Interplay between Plasmon and Single-Particle Excitations in a Metal Nanocluster. *Nat. Commun.* **2015**, *6*, No. 10107.

(14) Cortés, E.; Xie, W.; Cambiasso, J.; Jermyn, A. S.; Sundararaman, R.; Narang, P.; Schlücker, S.; Maier, S. A. Plasmonic Hot Electron Transport Drives Nano-Localized Chemistry. *Nat. Commun.* **2017**, *8*, No. 14880.

(15) Mukherjee, S.; Zhou, L.; Goodman, A. M.; Large, N.; Ayala-Orozco, C.; Zhang, Y.; Nordlander, P.; Halas, N. J. Hot-Electron-Induced Dissociation of H_2 on Gold Nanoparticles Supported on SiO_2. *J. Am. Chem. Soc.* **2014**, *136*, 64−67.

(16) Zhou, L.; Zhang, C.; McClain, M. J.; Manjavacas, A.; Krauter, C. M.; Tian, S.; Berg, F.; Everitt, H. O.; Carter, E. A.; Nordlander, P.; Halas, N. J. Aluminum Nanocrystals as a Plasmonic Photocatalyst for Hydrogen Dissociation. *Nano Lett.* **2016**, *16*, 1478−1484.

(17) Christopher, P.; Xin, H.; Linic, S. Visible-Light-Enhanced Catalytic Oxidation Reactions on Plasmonic Silver Nanostructures. *Nat. Chem.* **2011**, *3*, 467.

(18) Wang, R.; Kurouski, D. Elucidation of Tip-Broadening Effect in Tip-Enhanced Raman Spectroscopy (Ters): A Cause of Artifacts or Potential for 3D TERS. *J. Phys. Chem. C* **2018**, *122*, 24334−24340.

(19) Zhong, J. H.; Jin, X.; Meng, L.; Wang, X.; Su, H. S.; Yang, Z. L.; Williams, C. T.; Ren, B. Probing the Electronic and Catalytic Properties of a Bimetallic Surface with 3 nm Resolution. *Nat. Nanotechnol.* **2017**, *12*, 132−136.

(20) Kazuma, E.; Jung, J.; Ueba, H.; Trenary, M.; Kim, Y. Real-Space and Real-Time Observation of a Plasmon-Induced Chemical Reaction of a Single Molecule. *Science* **2018**, *360*, 521−526.

(21) Tesema, T. E.; Annesley, C.; Habteyes, T. G. Plasmon-Enhanced Autocatalytic N-Demethylation. *J. Phys. Chem. C* **2018**, *122*, 19831−19841.

(22) Li, X.; Zhang, C.; Wu, Q.; Zhang, J.; Xu, M.; Yuan, Y.; Yao, J. In Situ Surface-Enhanced Raman Spectroscopic Monitoring Electrochemical and Surface Plasmon Resonance Synergetic Catalysis on Dehydroxylation of PHTP at Ag Electrodes. *J. Raman Spectrosc.* **2018**, *49*, 1928−1937.

(23) Zheng, L. Q.; Yang, S.; Lan, J.; Gyr, L.; Goubert, G.; Qian, H.; Aprahamian, I.; Zenobi, R. Solution Phase and Surface Photoisomerization of a Hydrazone Switch with a Long Thermal Half-Life. *J. Am. Chem. Soc.* **2019**, *141*, 17637−17645.

(24) Hayazawa, N.; Inouye, Y.; Sekkat, Z.; Kawata, S. Metallized Tip Amplification of near-Field Raman Scattering. *Opt. Commun.* **2000**, *183*, 333−336.
(25) Domke, K. F.; Pettinger, B. Tip-Enhanced Raman Spectroscopy of 6H-SiC with Graphene Adlayers: Selective Suppression of E1 Modes. *J. Raman Spectrosc.* **2009**, *40*, 1427−1433.
(26) Kurouski, D.; Deckert-Gaudig, T.; Deckert, V.; Lednev, I. K. Structure and Composition of Insulin Fibril Surfaces Probed by TERS. *J. Am. Chem. Soc.* **2012**, *134*, 13323−13329.
(27) van Schrojenstein Lantman, E. M.; Deckert-Gaudig, T.; Mank, A. J.; Deckert, V.; Weckhuysen, B. M. Catalytic processes monitored at the nanoscale with tip-enhanced Raman spectroscopy. *Nat. Nanotechnol.* **2012**, *7*, 583−586.
(28) Sun, M.; Zhang, Z.; Kim, Z. H.; Zheng, H.; Xu, H. Plasmonic Scissors for Molecular Design. *Chem. − Eur. J.* **2013**, *19*, 14958−14962.
(29) Szczerbiński, J.; Gyr, L.; Kaeslin, J.; Zenobi, R. Plasmon-Driven Photocatalysis Leads to Products Known from E-Beam and X-Ray-Induced Surface Chemistry. *Nano Lett.* **2018**, *18*, 6740−6749.
(30) Tallarida, N.; Lee, J.; Apkarian, V. A. Tip-Enhanced Raman Spectromicroscopy on the Angstrom Scale: Bare and Co-Terminated Ag Tips. *ACS Nano* **2017**, *11*, 11393−11401.
(31) Lipiec, E.; Perez-Guaita, D.; Kaderli, J.; Wood, B. R.; Zenobi, R. Direct Nanospectroscopic Verification of the Amyloid Aggregation Pathway. *Angew. Chem., Int. Ed.* **2018**, *57*, 8519−8524.
(32) Apra, E.; Bhattarai, A.; Baxter, E.; Johnson, G. E.; Govind, N.; El-Khoury, P. Z. A Simplified Approach to Simulating Raman Spectra from Ab Initio Molecular Dynamics. arXiv:1909.03142.
(33) Valiev, M.; et al. NWChem: A Comprehensive and Scalable Open-Source Solution for Large Scale Molecular Simulations. *Comput. Phys. Commun.* **2010**, *181*, 1477−1489.
(34) Kim, H. J.; Yoon, J. H.; Yoon, S. Photooxidative Coupling of Thiophenol Derivatives to Disulfides. *J. Phys. Chem. A* **2010**, *114*, 12010−12015.
(35) Marr, J. M.; Schultz, Z. D. Imaging Electric Fields in Sers and Ters Using the Vibrational Stark Effect. *J. Phys. Chem. Lett.* **2013**, *4*, 3268−3272.
(36) Gieseking, R. L. M.; Lee, J.; Tallarida, N.; Apkarian, V. A.; Schatz, G. C. Bias-Dependent Chemical Enhancement and Nonclassical Stark Effect in Tip-Enhanced Raman Spectromicroscopy of Co-Terminated Ag Tips. *J. Phys. Chem. Lett.* **2018**, *9*, 3074−3080.
(37) Oklejas, V.; Sjostrom, C.; Harris, J. M. Sers Detection of the Vibrational Stark Effect from Nitrile-Terminated Sams to Probe Electric Fields in the Diffuse Double-Layer. *J. Am. Chem. Soc.* **2002**, *124*, 2408−2409.
(38) Banik, M.; El-Khoury, P. Z.; Nag, A.; Rodriguez-Perez, A.; Guarrottxena, N.; Bazan, G. C.; Apkarian, V. A. Surface-Enhanced Raman Trajectories on a Nano-Dumbbell: Transition from Field to Charge Transfer Plasmons as the Spheres Fuse. *ACS Nano* **2012**, *6*, 10343−10354.
(39) Marr, J. M.; Schultz, Z. D. Imaging Electric Fields in SERS and TERS Using the Vibrational Stark Effect. *J. Phys. Chem. Lett.* **2013**, *4*, 3268−3272.
(40) Ward, D. R.; Huser, F.; Pauly, F.; Cuevas, J. C.; Natelson, D. Optical Rectification and Field Enhancement in a Plasmonic Nanogap. *Nat. Nanotechnol.* **2010**, *5*, 732−736.
(41) Crampton, K. T.; Lee, J.; Apkarian, V. A. Ion-Selective, Atom-Resolved Imaging of a 2D Cu2N Insulator: Field and Current Driven Tip-Enhanced Raman Spectromicroscopy Using a Molecule-Terminated Tip. *ACS Nano* **2019**, *13*, 6363−6371.
(42) Wang, H.; Yao, K.; Parkhill, J. A.; Schultz, Z. D. Detection of electron tunneling across plasmonic nanoparticle−film junctions using nitrile vibrations. *Phys. Chem. Chem. Phys.* **2017**, *19*, 5786−5796.
(43) Fried, S. D.; Boxer, S. G. Measuring Electric Fields and Noncovalent Interactions Using the Vibrational Stark Effect. *Acc. Chem. Res.* **2015**, *48*, 998−1006.
(44) BAND2018 S. *Theoretical Chemistry*; Vrije Universiteit: Amsterdam, The Netherlands, http://www.scm.com.
(45) Kendall, R. A.; Früchtl, H. A. The impact of the resolution of the identity approximate integral method on modern ab initio algorithm development. *Theor. Chem. Acc.* **1997**, *97*, 158−163.
(46) Weigend, F. Accurate Coulomb-fitting basis sets for H to Rn. *Phys. Chem. Chem. Phys.* **2006**, *8*, 1057−1065.
(47) Nesse, F. The ORCA program system. *Wiley Interdiscip. Rev.: Comput. Mol. Sci.* **2012**, *2*, 73−78.
(48) Lumerical Solutions, Inc. https://www.lumerical.com/tcad-products/fdtd/.
(49) Lumerical Solutions, Inc. http://www.lumerical.com/tcad-products/device/.
(50) Brongersma, M. L.; Halas, N. J.; Nordlander, P. Plasmon-Induced Hot Carrier Science and Technology. *Nat. Nanotechnol.* **2015**, *10*, 25−34.
(51) Kazuma, E.; Kim, Y. Mechanistic Studies of Plasmon Chemistry on Metal Catalysts. *Angew. Chem., Int. Ed.* **2019**, *58*, 4800−4808.
(52) Funk, S.; Bonn, M.; Denzler, D. N.; Hess, C.; Wolf, M.; Ertl, G. Desorption of Co from Ru(001) Induced by near-Infrared Femtosecond Laser Pulses. *J. Chem. Phys.* **2000**, *112*, 9888−9897.
(53) Hertz, H. Ueber Einen Einfluss Des Ultravioletten Lichtes Auf Die Electrische Entladung. *Ann. Phys. Chem.* **1887**, *267*, 983−1000.
(54) Einstein, A. Über Einen Die Erzeugung Und Verwandlung Des Lichtes Betreffenden Heuristischen Gesichtspunkt. *Ann. Phys.* **1905**, *322*, 132−148.
(55) Gadzuk, J. W. Resonance-Assisted, Hot-Electron-Induced Desorption. *Surf. Sci.* **1995**, *342*, 345−358.
(56) Gadzuk, J. W.; Clark, C. W. Resonance Enhanced Electron Stimulated Desorption. *J. Chem. Phys.* **1989**, *91*, 3174−3181.
(57) Ashcroft, N. W.; Mermin, N. D. *Solid State Physics*; Saunders College: Philadelphia, PA, 1976.

https://dx.doi.org/10.1021/acs.jpcc.9b12002
J. Phys. Chem. C XXXX, XXX, XXX−XXX